

Behaviour of the Serre Equations in the Presence of Steep Gradients Revisited

J.P.A. Pitt^{a,*}, C. Zoppou^a, S.G. Roberts^a

^a*Mathematical Sciences Institute, Australian National University, Canberra, ACT 0200, Australia*

Abstract

We use various numerical methods to study the behaviour of the Serre equations in the presence of steep gradients, due to the lack of known analytical solutions for these problems. In keeping with the literature we study a class of initial condition problems that are a smooth approximation to the initial conditions of the dam-break problem. This class of initial condition problems allow us to observe the effect of varying steepness of the initial conditions on the solution of the Serre equations. To approximate the solution of the Serre equations we use numerical solutions from various methods. These numerical solutions are justified by demonstrating that as the resolution increases they converge to a numerical solution with littler error in conservation, independent of the numerical method. We find four different structures of the converged numerical solutions depending on the steepness of the initial conditions, two of which can be found in the literature with the other two not being commonly found in the literature for these equations. The numerical solutions are then used to assess how well the analytical solutions of the shallow water wave equations to the dam-break problem capture the mean behaviour of the solution of the Serre equations to the dam-break problem. Lastly the numerical solutions are used to evaluate the usefulness of asymptotic results in the literature to approximate the depth and location of the front of an undular bore.

Keywords: Serre equations, steep gradients, dam break

¹ 1. Introduction

² The behaviour of flows containing steep gradients are important to a range of prob-
³ lems in shallow water such as the propagation of a bore, the dam-break problem and
⁴ shoaling waves on a beach.

⁵ The Serre equations are used as a compromise between the non-dispersive shallow
⁶ water wave equations and the incompressible inviscid Euler equations for modelling
⁷ this behaviour. The Serre equations produce dispersive waves in the presence of steep

*Corresponding author

Email addresses: jordan.pitt@anu.edu.au (J.P.A. Pitt),
christopher.zoppou@anu.edu.au (C. Zoppou), stephen.roberts@anu.edu.au
(S.G. Roberts)

8 gradients as they do in the Euler equations [1]. However, unlike the Euler equations
9 there are efficient methods for solving the Serre equations [2–4], as there are for the
10 shallow water wave equations. The Serre equations are considered the most appro-
11 priate approximate model of dispersive waves up to the shore line [5, 6]. Therefore,
12 understanding the behaviour of the Serre equations in the presence of steep gradients
13 offers some insight into the behaviour of steep gradients for fluids more generally.

14 There are no known analytical solutions to problems containing steep gradients for
15 the Serre equations. To infer the structure of solutions to problems containing steep
16 gradients we have to resort to investigating numerical solutions of the Serre equations
17 for these problems.

18 Unfortunately, there are few examples in the literature which depict the behaviour
19 of numerical solutions to the Serre equations in the presence of steep gradients [1–
20 4, 7, 8]. These papers all present problems with discontinuous initial conditions [2–4]
21 or a smooth approximation to them [1, 7, 8]. Among these papers there are differences
22 in the structures of the numerical solutions, with some demonstrating undulations in
23 depth and velocity throughout the bore [3, 4, 7] and others showing a constant depth
24 and velocity state in the middle of the bore [1, 2, 8].

25 The mean behaviour of numerical solutions to the dam-break problem for the Serre
26 equations is consistent across the literature [1–4, 7, 8] and was demonstrated to be
27 well approximated by the analytical solution of the dam-break problem for the shallow
28 water wave equations [2, 8]. Expressions for the leading wave height and speed of an
29 undular bore for the Serre equations were derived and verified for a range of undular
30 bores by El et al. [7]. These expressions were also shown to be valid for the different
31 structures found in the literature [7, 8].

32 The first aim of this paper is to investigate and determine the cause of the different
33 behaviour that has been published in the literature for numerical solutions of the Serre
34 equations for problems containing steep gradients. We find that the undulations of a
35 bore can be damped to a constant depth and velocity state by the numerical diffusion
36 introduced by the method, as is the case for Le Métayer et al. [2]. Oscillation damping
37 can also occur due to the particular smoothing of the initial conditions, as is the case
38 for Mitsotakis et al. [1], El et al. [7] and Mitsotakis et al. [8].

39 The second aim of this paper is to assess the utility of the shallow water wave
40 equations and the results of El et al. [7] as guides for the evolution of an undular bore.
41 We find that for a range of dam-break problems the analytical solution of the shallow
42 water wave equations is a good approximation for the mean depth and velocity of the
43 Serre equations, extending the findings of Le Métayer et al. [2] and Mitsotakis et al.
44 [8] to a larger range of dam-break problems. It was also found that the results of El
45 et al. [7] are a good approximation to our numerical solutions and are only a slight
46 underestimation.

47 The first aim of this paper is achieved by demonstrating that our numerical solutions
48 are good approximations to the true solutions of the Serre equations. This is accom-
49 plished by demonstrating that as the resolution of a particular method is increased, the
50 numerical solutions converge to a numerical solution with little error in conservation,
51 and that this numerical solution is the same across the five different numerical meth-
52 ods. Three of the methods are the first, second and third-order methods presented by
53 Zoppou et al. [4]. The first-order method is equivalent to the method of Le Métayer

et al. [2]. The fourth method is a recreation of the second-order method used by El et al. [7]. Lastly, the fifth method is a second-order finite difference approximation to the Serre equations.

The second aim is accomplished by comparing our verified numerical solutions to the analytical solutions of the shallow water wave equations and the Whitham modulation results.

The paper is organised as follows, in Section 2 the Serre equations and the quantities they conserve are presented. In Section 3 the smoothed dam-break problem is defined, the measures of the relative difference between numerical solutions and the relative error in conservation are given. The analytical solution of the shallow water wave equations and the expressions for the amplitude and speed of the leading wave of an undular bore are given. In Section 4 the numerical methods and their important properties are presented. In Section 5 the four different structures in the solutions of smoothed dam-break problem for the Serre equations are determined using verified numerical solutions. The verified numerical solutions are also used to evaluate how well the analytical solution of the shallow water wave equations captures the mean behaviour of the solution of the Serre equations for the dam-break problem. The Whitham modulations results are also compared to the verified numerical solutions to test their veracity. Lastly, the Appendix presents the two finite difference methods in replicable detail.

2. Serre Equations

The Serre equations can be derived by integrating the full inviscid incompressible Euler equations over the water depth [9]. They can also be derived as an asymptotic expansion of the Euler equations [10]. Assuming a constant horizontal bed, the one-dimensional Serre equations are [11]

$$\frac{\partial h}{\partial t} + \frac{\partial(uh)}{\partial x} = 0 \quad (1a)$$

and

$$\underbrace{\frac{\partial(uh)}{\partial t} + \frac{\partial}{\partial x} \left(u^2 h + \frac{gh^2}{2} \right)}_{\text{Shallow Water Wave Equations}} + \underbrace{\frac{\partial}{\partial x} \left(\frac{h^3}{3} \left[\frac{\partial u}{\partial x} \frac{\partial u}{\partial x} - u \frac{\partial^2 u}{\partial x^2} - \frac{\partial^2 u}{\partial x \partial t} \right] \right)}_{\text{Dispersion Terms}} = 0. \quad (1b)$$

Serre Equations

Where $u(x, t)$ is the horizontal velocity over the depth of water $h(x, t)$, g is the acceleration due to gravity, x is the horizontal spatial variable and t is time.

The Serre equations are conservation laws for ‘mass’ (1a), ‘momentum’ (1b) and the Hamiltonian [12, 13]

$$\mathcal{H}(x, t) = \frac{1}{2} \left(hu^2 + \frac{h^3}{3} \left(\frac{\partial u}{\partial x} \right)^2 + gh^2 \right) \quad (2)$$

which is the total energy.

91 The total amount of a quantity q in a system in the spatial interval $[a, b]$ at a partic-
 92 ular time t , is measured by

$$93 \quad C_q(t) = \int_a^b q(x, t) dx.$$

95 Conservation of a quantity q implies that $C_q(0) = C_q(t)$ for all t provided the interval is
 96 fixed and the system is closed. Our numerical methods should demonstrate conserva-
 97 tion for the quantities h , uh and \mathcal{H} .

98 3. Smoothed Dam Break Problem

99 In this section we define a class of initial condition problems, called the smoothed
 100 dam-break problem that we use throughout our numerical investigation. This class of
 101 initial conditions are used in the literature [1, 8] to smoothly approximate the discon-
 102 tinuous initial conditions of the dam-break problem. There is, no analytical solutions
 103 of the Serre equations for the dam-break problem or an arbitrary smoothed dam-break
 104 problem. To demonstrate that our numerical solutions converge we use the relative
 105 difference between numerical solutions. To demonstrate that our numerical solutions
 106 have small errors in conservation we use the relative error in conservation. Both of
 107 these measures are defined in this section.

108 The smoothed dam-break problem has the following initial conditions

$$109 \quad h(x, 0) = h_0 + \frac{h_1 - h_0}{2} \left(1 + \tanh\left(\frac{x_0 - x}{\alpha}\right) \right) m, \quad (3a)$$

111 and

$$112 \quad u(x, 0) = 0.0 \text{ m/s}. \quad (3b)$$

114 This represents a smooth transition centred around x_0 between a water depth of h_0
 115 on the right and a water depth of h_1 on the left. Here α measures the distance over
 116 which approximately 46% of that smooth transition between the two heights occurs.
 117 Decreasing α increases the steepness of the initial conditions as can be seen in Figure
 118 1 where $h_0 = 1m$ and $h_1 = 1.8m$. These are the same h_0 and h_1 values as those of the
 119 smoothed dam-break problem of El et al. [7] and the dam-break problem of Le Métayer
 120 et al. [2].

121 3.1. Assessing validity of Numerical Solutions

122 To demonstrate that our numerical solutions converge to a solution with little error
 123 in conservation as the spatial resolution is increased we use two measures; the rela-
 124 tive difference between numerical solutions of different resolutions and the error in
 125 conservation. The relative difference between numerical solutions measures their con-
 126 vergence, while the error in conservation measures how well the numerical solutions
 127 conserve the quantities h , uh and \mathcal{H} .

128 We introduce the following notation for the spatial grids defined by x_i and the
 129 temporal grids defined by t^n upon which the numerical solutions are calculated. These

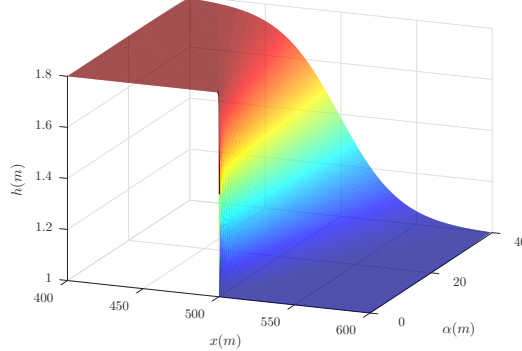


Figure 1: Initial conditions for smooth dam-break problems with $h_0 = 1m$, $h_1 = 1.8m$, $x_0 = 500m$ and various α .

130 grids are uniform so that $\Delta x = x_i - x_{i-1}$ for all i and $\Delta t = t^n - t^{n-1}$ for all n . We use
 131 subscripts and superscripts to denote where a quantity q is evaluated in the following
 132 way $q_i^n = q(x_i, t^n)$. Finally, the i th cell is the interval $[x_i - \Delta x/2, x_i + \Delta x/2]$ centred
 133 around x_i .

134 *3.1.1. Convergence of Numerical Results*

135 In these experiments, Δx was reduced by dividing it by 2 thus the finest grid with
 136 the smallest Δx contains all the locations x_i in any coarser grid. To measure the relative
 137 difference between quantities on these grids we compare them only on the coarser grid
 138 points x_i . For some quantity q we have our numerical approximation to it on the finest
 139 grid q^* and on the coarser grid q' , with the relative difference between the two being

$$140 \quad L_1^q = \frac{\sum_i |q'(x_i) - q^*(x_i)|}{\sum_i |q^*(x_i)|}. \quad (4)$$

142 *3.1.2. Conserved Quantities*

143 In the smoothed dam-break problem, the initial conditions (3) were integrated to get
 144 expressions for the total mass $C_h(0)$, the total momentum $C_{uh}(0)$ and the total Hamil-
 145 tonian $C_{\mathcal{H}}(0)$. Provided x_0 is the midpoint of the spatial domain $[a, b]$ the totals for the
 146 conserved quantities are

$$147 \quad C_h(0) = \frac{h_1 + h_0}{2} (b - a),$$

148

$$150 \quad C_{uh}(0) = 0$$

152 and

$$153 \quad C_{\mathcal{H}}(0) = \frac{g}{4} \left(h_0^2 - h_1^2 + \alpha (h_1 - h_0)^2 \tanh \left(\frac{a - b}{2\alpha} \right) \right).$$

154

156 To calculate how well we approximate the total amount of a quantity q in our
 157 numerical solution we fit a quartic interpolant of the primitive variables h and u over a
 158 cell utilising neighbouring cells and then apply Gaussian quadrature with 3 points. The
 159 amount of q in each cell is summed across all cells to get the total amount of q in
 160 our numerical solution at time t , which we call $C_q^*(t)$. The error in conservation of a
 161 quantity q for a numerical solution is

$$162 \quad C_1^q = \frac{|C_q(0) - C_q^*(t)|}{|C_q(0)|}. \quad (6)$$

164 Note that for uh the denominator is 0 and that there is a flux of momentum due to the
 165 unequal heights at both ends of the domain. To resolve these issues for uh the error in
 166 the conservation of uh is measured by

$$167 \quad C_1^{uh} = \left| C_{uh}(0) - C_{uh}^*(t) - \frac{gt}{2} (h(b)^2 - h(a)^2) \right|. \quad (7)$$

169 3.2. Background for derived and observed comparisons

170 It was demonstrated by Le Métayer et al. [2] and Mitsotakis et al. [8] that the
 171 analytical solution of the shallow water wave equations for the dam-break problem
 172 captures the mean behaviour of the numerical solutions of the Serre equations to the
 173 dam-break problem [2] and the smoothed dam-break problem [8].

174 El et al. [7] derived an expression for the long term amplitude of the leading wave
 175 of an undular bore A^+ for the Serre equations. Since the front of an undular bore
 176 decomposes into solitons, the speed of the leading wave can be calculated from its
 177 amplitude.

178 To be self contained we present the analytical solution of the shallow water wave
 179 equations to the dam-break problem and the expressions derived by El et al. [7].

180 3.2.1. Shallow Water Wave Equation Analytical Solution

181 For the dam-break problem the shallow water wave equations, which are the Serre
 182 equations with dispersive terms neglected, can be solved analytically.

183 An example of the analytical solution of the shallow water wave equations for the
 184 dam-break problem is presented in Figure 2. Region I is the undisturbed water up-
 185 stream of the dam-break at constant height (h_1) and velocity (0m/s). Region II is the
 186 rarefaction fan connecting regions I and III. regions III and IV are the constant height
 187 (h_2) and constant velocity (u_2) states which are separated by $x_{u_2} = x_0 + u_2 t$. Region V
 188 is the undisturbed water downstream at constant height (h_0) and velocity (0m/s) sep-
 189 arated from Region IV by a shock which travels at velocity S_2 . Expressions for the
 190 unknown quantities h_2 , u_2 and S_2 in terms of h_0 and h_1 were given by Wu et al. [14] as

$$191 \quad h_2 = \frac{h_0}{2} \left(\sqrt{1 + 8 \left(\frac{2h_2}{h_2 - h_0} \frac{\sqrt{h_1} - \sqrt{h_2}}{\sqrt{h_0}} \right)^2} - 1 \right), \quad (8a)$$

$$194 \quad u_2 = 2 \left(\sqrt{gh_1} - \sqrt{gh_2} \right) \quad (8b)$$

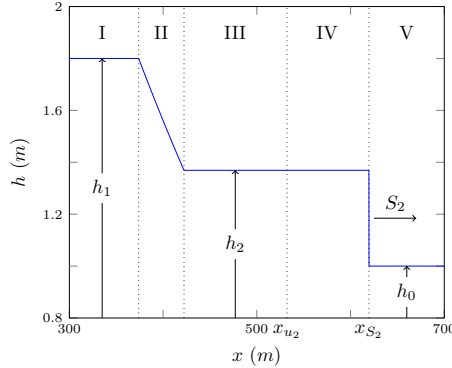


Figure 2: Analytical solution at $t = 30s$ of the dam-break problem for the shallow water wave equations with $h_0 = 1m$, $h_1 = 1.8m$ and $x_0 = 500m$.

196 and

$$197 \quad 198 \quad S_2 = \frac{h_2 u_2}{h_2 - h_0}. \quad (8c)$$

199 Applying (8) to our dam-break heights of interest; $h_0 = 1m$ and $h_1 = 1.8m$ results
200 in $h_2 = 1.36898m$, $u_2 = 1.074975 m/s$ and $S_2 = 3.98835 m/s$ which are shown in
201 Figure 2 for $t = 30s$. The location of the front of the bore for the shallow water wave
202 equations at time t is thus $x_{S_2}(t) = x_0 + S_2 t$.

203 3.2.2. *Whitham Modulation for Undular Bores of the Serre Equations*

204 Utilizing Whitham modulation theory for a one-phase periodic travelling wave an
205 asymptotic analytical expression for the amplitude A^+ and speed S^+ of the leading
206 wave was derived by El et al. [7]. An example of an undular bore is shown in Figure 3.
207 The derived expressions for A^+ and S^+ are

$$208 \quad 209 \quad \frac{\Delta}{(A^+ + 1)^{1/4}} - \left(\frac{3}{4 - \sqrt{A^+ + 1}} \right)^{21/10} \left(\frac{2}{1 + \sqrt{A^+ + 1}} \right)^{2/5} = 0 \quad (9a)$$

210 and

$$\frac{211}{212} \quad S^+ = \sqrt{g(A^+ + 1)} \quad (9b)$$

where $\Delta = h_b/h_0$, and h_b is the height of the bore. The height of the bore created by
the dam-break problem in (9a) used by El et al. [7] was

$$h_b = \frac{1}{4} \left(\sqrt{\frac{h_1}{h_0}} + 1 \right)^2.$$

213 For our dam-break heights of interest $h_0 = 1m$ and $h_1 = 1.8m$ we obtain $h_b = 1.37082m$, $\Delta = 1.37082$, $A^+ = 1.73998m$ and $S^+ = 4.13148m/s$. The location of
214 the leading wave of an undular bore at time t is then $x_{S^+}(t) = x_0 + S^+ t$.
215

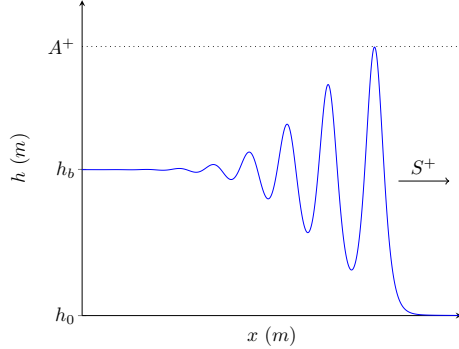


Figure 3: Demonstration of quantities obtained by Whitham modulation for undular bores of the Serre equations.

216 4. Numerical Methods

217 Five numerical schemes are used to investigate the behaviour of the Serre equations
 218 in the presence of steep gradients. The first (\mathcal{V}_1), second (\mathcal{V}_2) and third-order (\mathcal{V}_3)
 219 finite difference finite volume methods of Zoppou et al. [4]. The second-order finite
 220 difference method of El et al. [7] (\mathcal{E}) and a second-order finite difference method (\mathcal{D})
 221 that can be found in the Appendix.

222 The \mathcal{V}_i methods are stable under a Courant-Friederichs-Lowy (CFL) condition
 223 such as the one presented by A. Harten [15]. The \mathcal{V}_i methods have demonstrated
 224 the appropriate order of convergence for smooth problems [4]. Furthermore, \mathcal{V}_2 and
 225 \mathcal{V}_3 have been validated against experimental data containing steep gradients [4]. The
 226 two methods \mathcal{D} and \mathcal{E} were found to be stable under the CFL condition as well.

227 Generally, we found that \mathcal{V}_1 is the worst performing method due to its numeri-
 228 cal diffusion [4]. Of the high-order methods \mathcal{E} is the worst performing, introducing
 229 dispersive errors.

230 5. Numerical Results

231 We investigate the behaviour of the Serre equations in the presence of steep gradi-
 232 ents by numerically solving the smoothed dam-break problem while varying the steep-
 233 ness of the initial conditions. As $\Delta x \rightarrow 0$ our numerical solutions should better ap-
 234 proximate the true solution of the Serre equations. If our numerical solutions to a
 235 smoothed dam-break problem converge to the same numerical solution with little error
 236 in conservation as $\Delta x \rightarrow 0$ for each method, then this numerical solution is considered
 237 an accurate approximate solution to that smoothed dam-break problem for the Serre
 238 equations.

239 This process validates our numerical solutions for the smoothed dam-break prob-
 240 lem, and thus validates our numerical methods to approximate the solution of the Serre
 241 equations in the presence of steep gradients. With a validated model we can compare
 242 the numerical solution to the analytical solution of the shallow water wave equations
 243 for the dam-break problem and the results of El et al. [7].

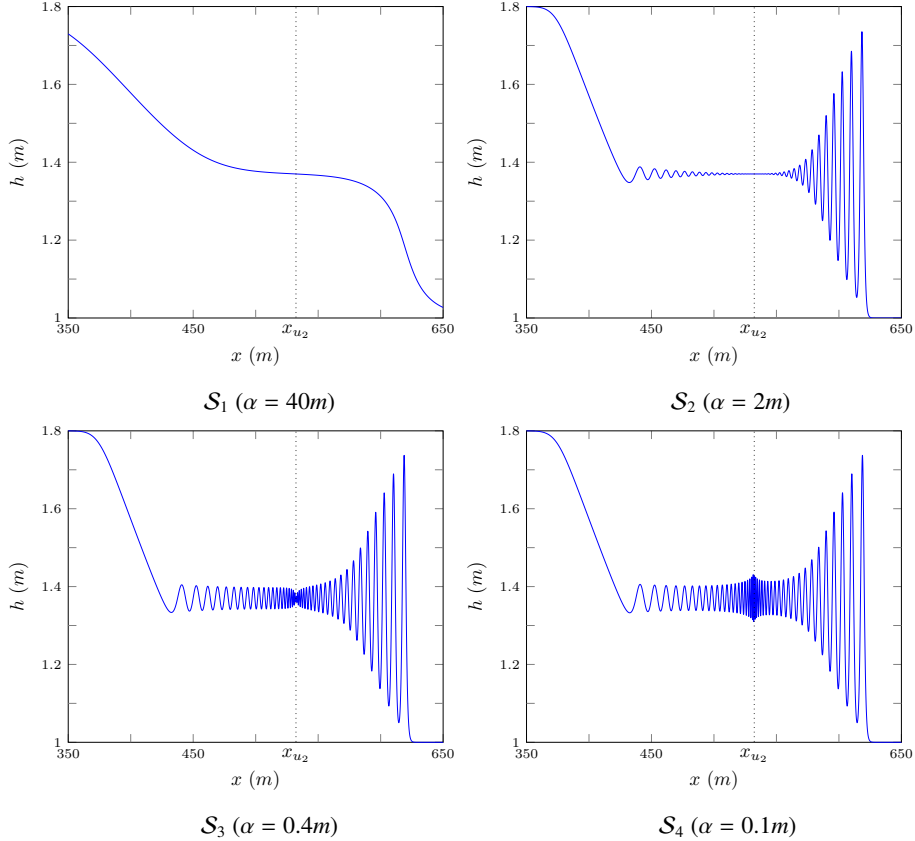


Figure 4: Numerical results of \mathcal{V}_3 with $\Delta x = 10/2^{11}m$ (—) at $t = 30s$ for various smooth dam-break problems demonstrating the different observed structures.

Throughout most of this section we are interested in the numerical solution at $t = 30s$ to the smoothed dam-break problem with $h_0 = 1m$, $h_1 = 1.8m$ and $x_0 = 500m$ while allowing for different α values. All numerical methods used $\Delta t = 0.01\Delta x$ which is smaller than required by the CFL condition, ensuring stability of our schemes. The method \mathcal{V}_2 requires an input parameter to its slope limiter and this was chosen to be $\theta = 1.2$ [4]. The spatial domain was $[0m, 1000m]$ with the following Dirichlet boundary conditions, $u = 0m/s$ at both boundaries, $h = 1.8m$ on the left and $h = 1m$ on the right.

5.1. Observed Structures of the Numerical Solutions

We observe that there are four different structures for the converged to numerical solution depending on the chosen α . They are the ‘non-oscillatory’ structure \mathcal{S}_1 , the ‘flat’ structure \mathcal{S}_2 , the ‘node’ structure \mathcal{S}_3 and the ‘growth’ structure \mathcal{S}_4 . An example of each of these structures is shown in Figure 4 which were obtained using \mathcal{V}_3 with $\Delta x = 10/2^{11}m$.

The four structures are identified by the dominant features of the numerical solutions in regions III and IV. They correspond to different structures in the numerical

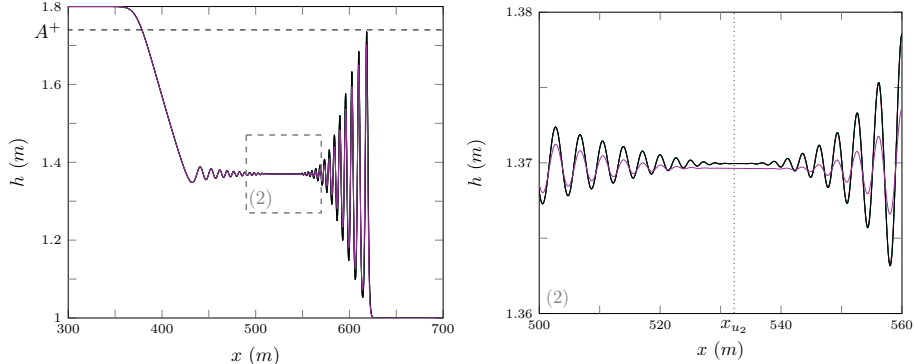


Figure 5: Numerical solutions of \mathcal{D} (blue), \mathcal{E} (red), \mathcal{V}_3 (green), \mathcal{V}_2 (black) and \mathcal{V}_1 (purple) with $\Delta x = 10/2^{11}m$ at $t = 30s$ for the smooth dam-break problem with $\alpha = 2m$.

solutions that have been presented in the literature. From Figure 4 it can be seen that as α is decreased, steepening the initial conditions, the numerical solutions demonstrate an increase in the size and number of oscillations particularly around x_{u_2} . We observe that the difference between \mathcal{S}_2 , \mathcal{S}_3 and \mathcal{S}_4 is the amplitude of the oscillations in regions III and IV.

For the non-oscillatory and flat structures there is excellent agreement between all higher-order numerical methods at our highest resolution $\Delta x = 10/2^{11}m$. An illustration of this agreement is given in Figure 5 for \mathcal{S}_2 which is the most difficult to resolve of the two structures. However, the first-order method \mathcal{V}_1 suppresses oscillations present in the numerical solutions of other methods due to its diffusive errors [4], requiring lower Δx to resolve them.

5.1.1. Non-oscillatory Structure

The \mathcal{S}_1 structure is the result of a large α , which causes the front of this flow to not be steep enough to generate undulations over short time periods. As the system evolves the front will steepen due to non-linearity and undulations will develop.

The structure \mathcal{S}_1 is not present in the literature as no authors chose large enough α , as such a large α poorly approximates the dam-break problem. An example of this structure can be seen in Figure 6 for $\alpha = 40m$ using \mathcal{V}_3 with various Δx values. Because this is not a very steep problem all numerical results are visually identical for all $\Delta x < 10/2^4m$.

From Table 1 it can be seen that not only have these solutions converged visually but the L_1 measures demonstrate that we have reached convergence to round-off error by $\Delta x = 10/2^8m$ after which the relative difference between numerical solutions plateau.

Table 1 also demonstrates that the error in conservation of the numerical solutions are at round-off error for h and \mathcal{H} . The conservation of uh is poor because the smoothed dam-break has such a large α that $h(0m) \neq 1.8m$ and $h(1000m) \neq 1m$, causing unequal fluxes in momentum at the boundaries.

As stated above when $\Delta x = 10/2^{11}m$ the numerical solutions from all methods are visually identical for this smoothed dam-break problem.

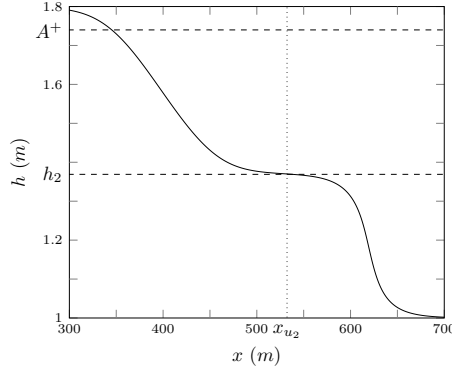


Figure 6: Numerical solutions of \mathcal{V}_3 at $t = 30s$ for smooth dam-break problem with $\alpha = 40m$ for $\Delta x = 10/2^{10}m$ (blue), $10/2^8m$ (red), $10/2^6m$ (green) and $10/2^4m$ (black).

288 The convergence of the numerical solutions as $\Delta x \rightarrow 0$ to a numerical solution
 289 with small error in conservation, independent of the method demonstrates that we have
 290 accurately solved the smoothed dam-break problem with $\alpha = 40m$. Therefore, the S_1
 291 structure should be observed in the solutions of the Serre equations for the smoothed
 292 dam-break problem for sufficiently large α .

293 *5.1.2. Flat Structure*

294 The most common structure observed in the literature [1, 2, 8] is the Flat structure,
 295 S_2 . It is observed when the initial conditions are steep enough such that the bore
 296 that develops has undulations. This structure consists of oscillations in regions III and
 297 IV which are separated by a constant height state around x_{u_2} . An example of the S_2
 298 structure can be seen in the numerical solutions presented in Figure 7 where $\alpha = 2m$.

299 As Δx decreases the numerical solutions converge so that by $\Delta x = 10/2^8m$ the solu-
 300 tions for higher Δx are visually identical. Table 1 demonstrates that although we have
 301 convergence visually, the L_1 measures are still decreasing and are larger than round-off
 302 error. Likewise the C_1 measures are still decreasing and have only reached round-off
 303 error for h . This indicates that to attain full convergence of the numerical solutions
 304 of this smoothed dam-break problem down to round-off error using \mathcal{V}_3 would require
 305 an even smaller Δx . The relative difference between numerical solutions is small and
 306 the numerical solutions exhibit good conservation. Therefore, our highest resolution
 307 numerical solution is a good approximation to any numerical solutions with lower Δx
 308 values. Furthermore, Figure 5 demonstrates that the highest resolution numerical solu-
 309 tion of all higher-order methods are the same.

310 Using \mathcal{V}_3 with $\Delta x = 10/2^{11}m$ we have not attained the desired full convergence
 311 of the numerical solutions to one with little conservation error, independent of the par-
 312 ticular method. However, we have demonstrated that we have obtained a very good
 313 approximation to such a numerical solution. Therefore, our highest resolution numeri-
 314 cal solution is an accurate approximate solution of the Serre equations for the smoothed
 315 dam-break problem with $\alpha = 2m$. Implying that the S_2 structure should be observed in
 316 solutions of the Serre equations for smooth dam-break problems with similar α values.

α	Δx	C_1^h	C_1^{uh}	C_1^H	L_1^h	L_1^u
40	$10/2^4$	$2.00 \cdot 10^{-11}$	$1.77 \cdot 10^{-6}$	$1.23 \cdot 10^{-8}$	$1.74 \cdot 10^{-7}$	$2.90 \cdot 10^{-6}$
40	$10/2^6$	$1.07 \cdot 10^{-11}$	$1.50 \cdot 10^{-6}$	$1.49 \cdot 10^{-10}$	$2.57 \cdot 10^{-9}$	$4.19 \cdot 10^{-8}$
40	$10/2^8$	$8.77 \cdot 10^{-13}$	$5.49 \cdot 10^{-7}$	$3.77 \cdot 10^{-13}$	$6.08 \cdot 10^{-11}$	$5.28 \cdot 10^{-10}$
40	$10/2^{10}$	$1.77 \cdot 10^{-11}$	$2.21 \cdot 10^{-8}$	$3.56 \cdot 10^{-11}$	$2.54 \cdot 10^{-11}$	$6.49 \cdot 10^{-11}$
<hr/>						
2	$10/2^4$	$4.90 \cdot 10^{-14}$	$5.10 \cdot 10^{-3}$	$8.69 \cdot 10^{-4}$	$5.02 \cdot 10^{-3}$	$6.77 \cdot 10^{-2}$
2	$10/2^6$	$2.51 \cdot 10^{-13}$	$2.18 \cdot 10^{-4}$	$6.58 \cdot 10^{-5}$	$4.14 \cdot 10^{-4}$	$5.20 \cdot 10^{-3}$
2	$10/2^8$	$9.81 \cdot 10^{-13}$	$7.72 \cdot 10^{-7}$	$5.01 \cdot 10^{-7}$	$6.00 \cdot 10^{-6}$	$7.59 \cdot 10^{-5}$
2	$10/2^{10}$	$3.95 \cdot 10^{-12}$	$5.56 \cdot 10^{-9}$	$6.13 \cdot 10^{-9}$	$1.76 \cdot 10^{-7}$	$2.33 \cdot 10^{-6}$
<hr/>						
0.4	$10/2^4$	$9.00 \cdot 10^{-14}$	$4.82 \cdot 10^{-3}$	$1.02 \cdot 10^{-3}$	$6.79 \cdot 10^{-3} \dagger$	$9.93 \cdot 10^{-2} \dagger$
0.4	$10/2^6$	$2.40 \cdot 10^{-13}$	$2.41 \cdot 10^{-4}$	$1.11 \cdot 10^{-4}$	$8.89 \cdot 10^{-4} \dagger$	$1.13 \cdot 10^{-2} \dagger$
0.4	$10/2^8$	$9.68 \cdot 10^{-13}$	$7.57 \cdot 10^{-7}$	$2.25 \cdot 10^{-6}$	$1.53 \cdot 10^{-5} \dagger$	$1.91 \cdot 10^{-4} \dagger$
0.4	$10/2^{10}$	$3.91 \cdot 10^{-12}$	$4.95 \cdot 10^{-9}$	$2.01 \cdot 10^{-8}$	$3.61 \cdot 10^{-7} \dagger$	$5.00 \cdot 10^{-6} \dagger$
<hr/>						
0.1	$10/2^4$	$7.60 \cdot 10^{-14}$	$4.82 \cdot 10^{-3}$	$1.06 \cdot 10^{-3}$	$7.04 \cdot 10^{-3} \dagger$	$1.02 \cdot 10^{-1} \dagger$
0.1	$10/2^6$	$2.40 \cdot 10^{-13}$	$2.39 \cdot 10^{-4}$	$1.44 \cdot 10^{-4}$	$1.02 \cdot 10^{-3} \dagger$	$1.28 \cdot 10^{-2} \dagger$
0.1	$10/2^8$	$9.79 \cdot 10^{-13}$	$2.21 \cdot 10^{-7}$	$1.20 \cdot 10^{-5}$	$2.86 \cdot 10^{-5} \dagger$	$3.46 \cdot 10^{-4} \dagger$
0.1	$10/2^{10}$	$3.92 \cdot 10^{-12}$	$4.46 \cdot 10^{-8}$	$7.61 \cdot 10^{-7}$	$4.99 \cdot 10^{-7} \dagger$	$6.40 \cdot 10^{-6} \dagger$

Table 1: All errors in conservation C_1^q for the conserved quantities and relative differences L_1^q of the primitive variables for numerical solutions of \mathcal{V}_3 . L_1^q uses the numerical solution with $\Delta x = 10/2^{11}m$ as the high resolution basis of comparison and \dagger indicates the omission of the interval $[520m, 540m]$ from the comparison.

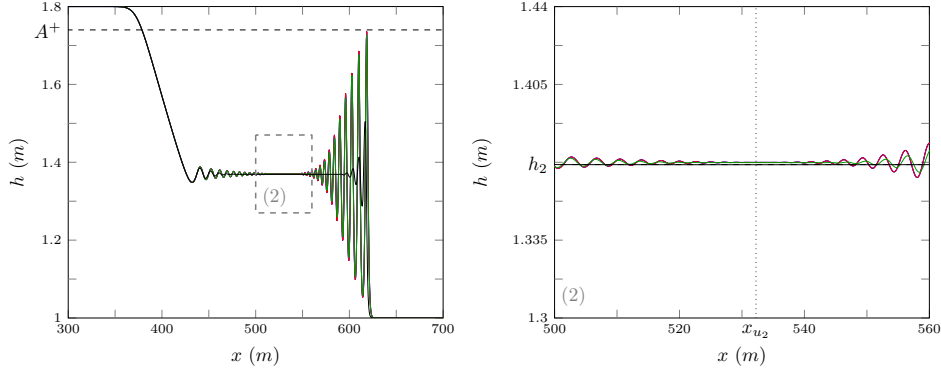


Figure 7: Numerical solutions of \mathcal{V}_3 at $t = 30s$ for the smooth dam-break problem with $\alpha = 2m$ for $\Delta x = 10/2^{10}m$ (—), $10/2^8m$ (—), $10/2^6m$ (—) and $10/2^4m$ (—).

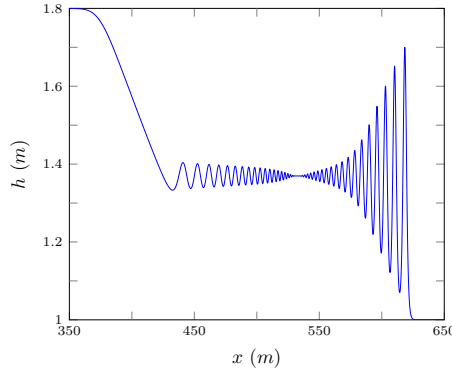


Figure 8: Numerical solution of \mathcal{V}_1 at $t = 30s$ for the smooth dam-break problem with $\alpha = 0.001m$ for $\Delta x = 10/2^{11}m$ (—).

317 These numerical solutions compare well with those of Mitsotakis et al. [8] who
 318 use the same α but different h_0 and h_1 values and observe the \mathcal{S}_2 structure. We found
 319 that we observed this structure for all numerical method's numerical solutions to the
 320 smoothed dam-break problem with α values as low as $1m$ and $\Delta x = 10/2^{11}m$. The
 321 numerical solutions of Mitsotakis et al. [1] use $\alpha = 1m$ but different heights and observe
 322 the structure \mathcal{S}_2 . Therefore Mitsotakis et al. [8] and Mitsotakis et al. [1] observe the \mathcal{S}_2
 323 structure in their numerical results due to their choice of α for the smoothed dam-break
 324 problem.

325 The first-order method \mathcal{V}_1 is diffusive [4] and damps oscillations that are present
 326 in the numerical solutions of higher-order methods as in Figure 5. We find that for any
 327 smoothed dam-break problem with $\alpha \leq 4m$ and the dam-break problem our numerical
 328 solutions with \mathcal{V}_1 at $t = 30s$ using $\Delta x = 10/2^{11}m$ only observe the \mathcal{S}_2 structure.
 329 This is evident in Figure 8 with the numerical solutions of \mathcal{V}_1 using our finest grid
 330 where $\Delta x = 10/2^{11}m$ for our steepest initial conditions where $\alpha = 0.001m$. Therefore,
 331 Le Métayer et al. [2] using the diffusive \mathcal{V}_1 with their chosen Δx and Δt , which are
 332 larger than our Δx and Δt could only observe the \mathcal{S}_2 structure.

333 5.1.3. *Node Structure*

334 The node structure, \mathcal{S}_3 was observed by El et al. [7]. The \mathcal{S}_3 structure has oscillations throughout regions III and IV that decay to a node at x_{u_2} as can be seen in Figure 9 where $\alpha = 0.4m$.

337 Figure 9 demonstrates that our numerical solutions have not converged, however
338 this is only in the area around x_{u_2} . Due to the large difference in numerical solutions
339 around x_{u_2} the L_1 measure over the area around x_{u_2} would not be insightful. However,
340 by omitting this region we can gain some knowledge about how well our solutions
341 agree away from x_{u_2} . This was performed for the relevant L_1 measures in Table 1
342 by omitting the interval $[520m, 540m]$. These modified L_1 measures demonstrate that
343 while our numerical results have visually converged outside this interval, they have not
344 converged down to round-off error.

345 Table 1 demonstrates that the C_1 measures are still decreasing and have only attained
346 round-off error for h . Therefore, to resolve the desired convergence of the numerical
347 solutions to one with small error in conservation using \mathcal{V}_3 would require even
348 smaller Δx values.

349 There is good agreement across different numerical methods for $\Delta x = 10/2^{11}m$ as
350 can be seen in Figure 10. In particular all the higher-order methods exhibit the same
351 structure and only disagree in a very small region around x_{u_2} . We observe that the
352 numerical solutions of the worst higher-order method \mathcal{E} has not converged well to the
353 numerical solutions of the other higher-order methods.

354 We have only obtained a good approximation to the desired numerical solution as
355 $\Delta x \rightarrow 0$ away from x_{u_2} . However, our highest resolution numerical solutions from
356 various higher-order methods are very similar. This suggests that again although we
357 do not have full convergence, our highest resolution numerical solution is a good ap-
358 proximation to the desired numerical solution over the whole domain. Therefore, our
359 highest resolution numerical solutions are an accurate representation of the solutions of
360 the Serre equations for this smoothed dam-break problem. Therefore, the \mathcal{S}_3 structure
361 should be observed in the solutions of the Serre equations for the smoothed dam-break
362 problem with $\alpha = 0.4m$.

363 These numerical solutions support the findings of El et al. [7] who also use some
364 smoothing [16] but do not report what smoothing was performed. Using their method
365 \mathcal{E} and similar Δx to El et al. [7] we observe the \mathcal{S}_4 “growth structure” in the numerical
366 solution for α values smaller than $0.1m$, indicating that the smoothing performed by El
367 et al. [7] limited their observed behaviour to just the \mathcal{S}_3 structure.

368 5.1.4. *Growth Structure*

369 The \mathcal{S}_4 “growth structure”, which has hitherto not been commonly published in
370 the literature features a growth in the oscillation amplitude around x_{u_2} . An example
371 of the growth structure can be seen for \mathcal{V}_3 ’s numerical solutions in Figure 11 to the
372 smoothed dam-break problem with $\alpha = 0.1m$. This structure was observed in the
373 numerical solutions of \mathcal{V}_3 for $\Delta x = 10/2^{11}m$ at $t = 30s$ for α values as low as $0.001m$
374 and even for the dam-break problem.

375 Figure 11 shows that this structure can only be observed for $\Delta x = 10/2^{10}m$, with
376 poor convergence of the numerical results around x_{u_2} . Again our L_1 measures in Table
377 1 omit the interval $[520m, 540m]$ in the numerical solutions. This demonstrates that

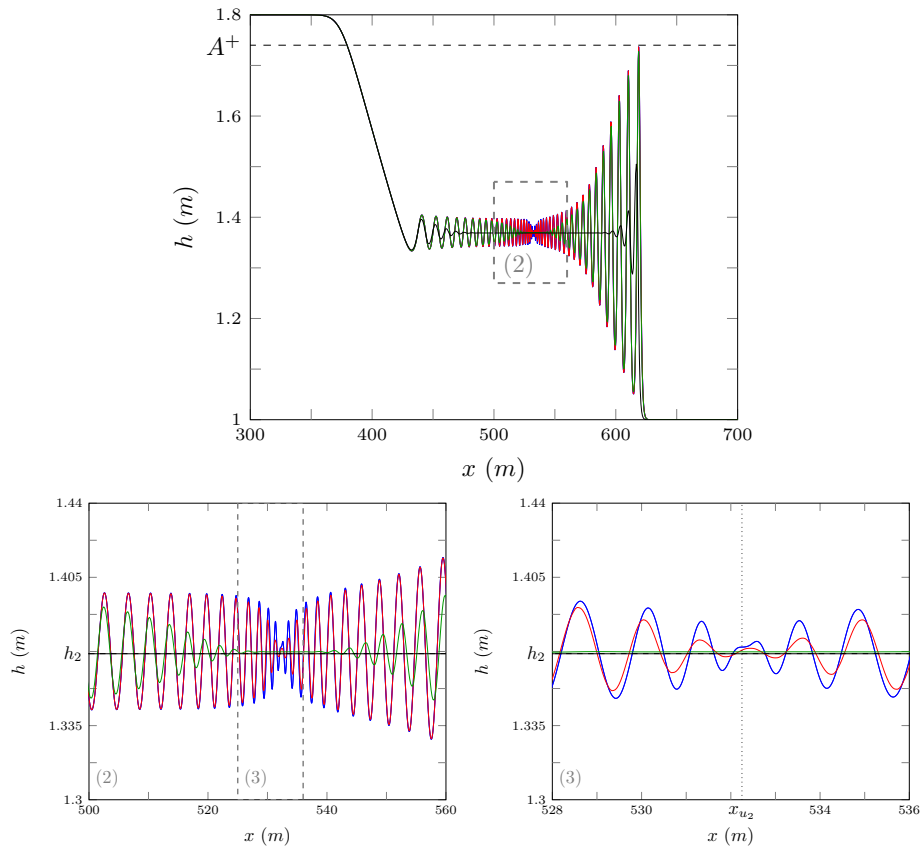


Figure 9: Numerical solutions of V_3 at $t = 30s$ for the smooth dam-break problem with $\alpha = 0.4m$ for $\Delta x = 10/2^{10}m$ (blue), $10/2^8m$ (red), $10/2^6m$ (green) and $10/2^4m$ (black).

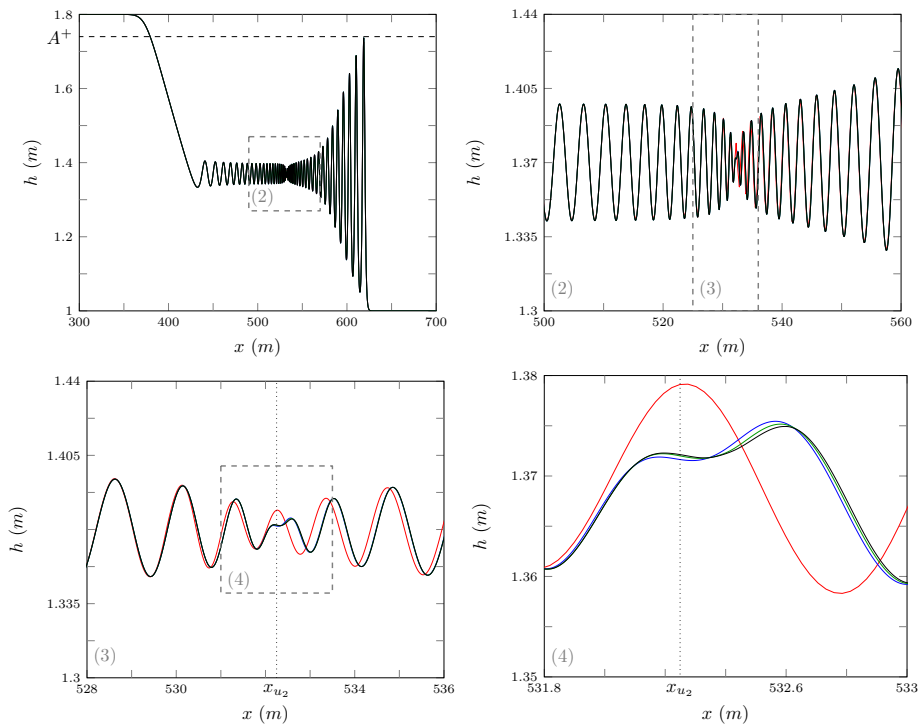


Figure 10: Numerical solutions of \mathcal{D} (—), \mathcal{E} (—), \mathcal{V}_3 (—) and \mathcal{V}_2 (—) at $t = 30s$ with $\Delta x = 10/2^{11}m$ for the smoothed dam-break problem with $\alpha = 0.4m$.

378 although we have visual convergence away from x_{u_2} our numerical solutions have not
379 converged to round-off error as $\Delta x \rightarrow 0$. The C_1 measures in Table 1 are still decreasing
380 and have only attained round-off error for h , although for uh and \mathcal{H} the errors in
381 conservation are small. These measures continue the trend in Table 1 where smaller
382 α 's and thus steeper initial conditions lead to larger L_1 and C_1 measures because these
383 problems are more difficult to solve accurately.

384 Figure 12 demonstrates that our numerical solutions for $\Delta x = 10/2^{11}m$ with the
385 best methods \mathcal{D} , \mathcal{V}_3 and \mathcal{V}_2 disagree for only a few oscillations around x_{u_2} . Since both
386 \mathcal{D} and \mathcal{E} are second-order finite difference methods their errors are dispersive. These
387 dispersive errors manifest in the numerical solutions of both methods as an increase
388 in the amplitude of oscillations particularly around x_{u_2} . Because the dispersive errors
389 of \mathcal{E} are larger than \mathcal{D} more oscillations are observed. The \mathcal{V}_3 method was shown to
390 be diffusive by Zoppou et al. [4] and therefore its numerical solutions underestimate
391 the size and number of oscillations. Therefore, the true solution of the Serre equations
392 should be between the dispersive method \mathcal{D} and the diffusive method \mathcal{V}_3 , and thus will
393 possess the \mathcal{S}_4 structure.

394 The numerical solutions of \mathcal{D} and \mathcal{V}_3 acting as upper and lower bounds respectively
395 for the oscillation amplitude as Δx is reduced is demonstrated in Figure 13 using
396 the maximum of h in the interval $[520m, 540m]$. From this figure it is clear that the
397 amplitudes of the numerical solutions of \mathcal{D} converge down to the limit as the resolution
398 is increased while the numerical solution amplitudes of \mathcal{V}_3 converge up to it. This
399 shows that we have effectively bounded the true solution of the Serre equations. Un-
400 fortunately, \mathcal{V}_3 could not be run in reasonable computational times with lower Δx , but
401 the numerical solutions of \mathcal{D} show that doing so is unnecessary.

402 These results indicate that the solutions of the Serre equations to the smoothed
403 dam-break problem with sufficiently small α values should exhibit a growth structure at
404 $t = 30s$, even though we have not precisely resolved all the oscillations in our numerical
405 solutions.

406 It was found that decreasing α did increase the amplitude of the oscillations around
407 x_{u_2} but not drastically. For \mathcal{V}_3 with $\Delta x = 10/2^{11}m$ and $\alpha = 0.001m$ the oscillations in
408 h were bounded by the interval $[1.28m, 1.46m]$. Of particular note is that the number of
409 oscillations are the same in Figures 10 and 12 for the best methods even though they
410 have different structures.

411 By changing the interval and desired time for the numerical solution, Δx could be
412 lowered further so that by $t = 3s$ our numerical solutions have reached full convergence
413 for α values as low as $0.001m$. This allows us to show that the height of the oscillations
414 for the solution of the Serre equation to the smoothed dam-break problem are bounded
415 at $t = 3s$ as $\alpha \rightarrow 0$. Figure 14 demonstrates this for the numerical solutions of \mathcal{V}_3 with
416 $\Delta x = 10/2^{13}m$.

417 5.2. Shallow water wave equation comparison

418 The analytical solutions of shallow water wave equations have been used as a guide
419 for the mean behaviour of the solution of the Serre equations for the dam-break problem
420 in the literature [2, 8].

421 To assess the applicability of this the mean bore depth and mean fluid velocity in
422 the interval $[x_{u_2} - 50m, x_{u_2} + 50m]$ were calculated from our numerical solution to the

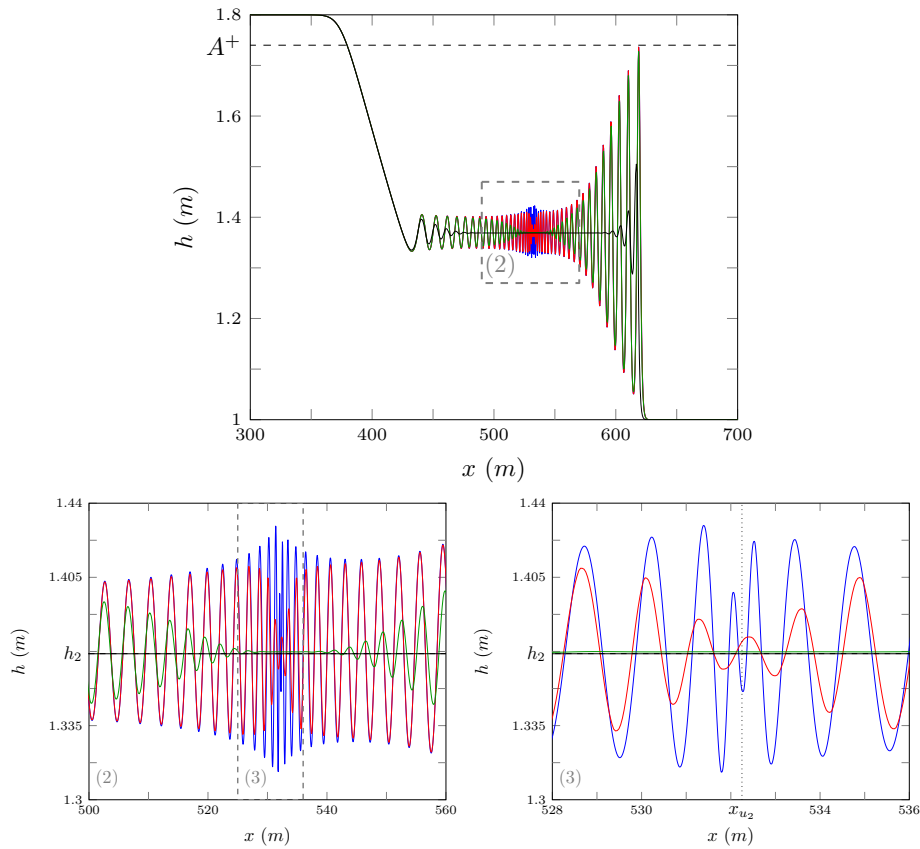


Figure 11: Numerical solutions of \mathcal{V}_3 at $t = 30s$ for the smooth dam-break problem with $\alpha = 0.1m$ for $\Delta x = 10/2^{10}m$ (blue), $10/2^8m$ (red), $10/2^6m$ (green) and $10/2^4m$ (black).

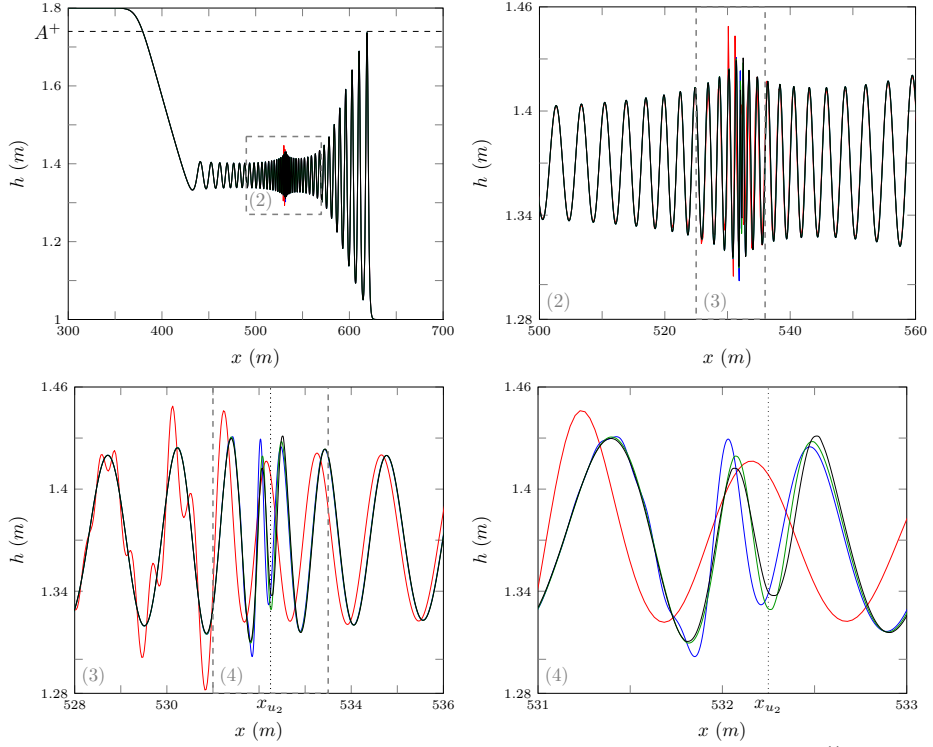


Figure 12: Numerical solutions of \mathcal{D} (blue solid), \mathcal{E} (red solid), \mathcal{V}_3 (green solid) and \mathcal{V}_2 (black solid) at $t = 30s$ with $\Delta x = 10/2^{11}m$ for the smoothed dam-break problem with $\alpha = 0.1m$.

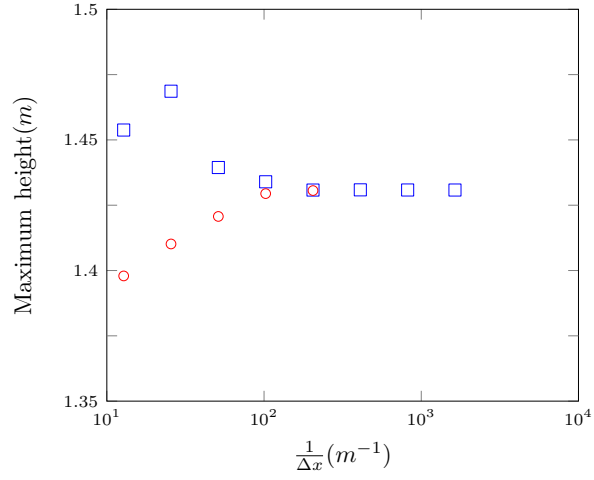


Figure 13: Maximum height of numerical solution of the smoothed dam-break problem with $\alpha = 0.4m$ at $t = 30s$ inside the interval [520m, 540m] using \mathcal{D} (□) and \mathcal{V}_3 (○).

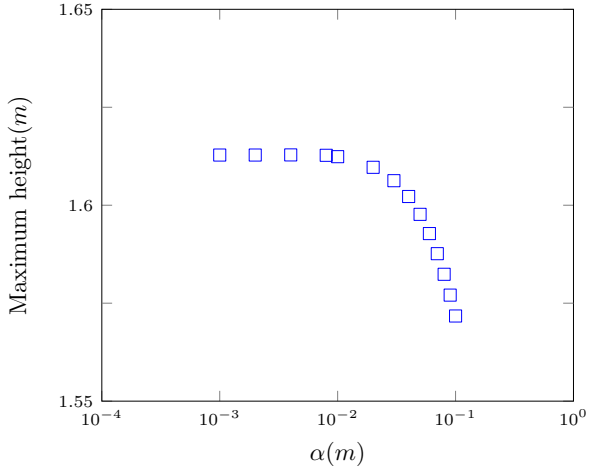


Figure 14: Maximum height of numerical solution around x_{u_2} at $t = 3s$ of various smoothed dam-break problem as α decreases, using \mathcal{V}_3 (□) with $\Delta x = 10/2^{13}m$.

smoothed dam-break problem with various height ratios. These means were compared to their approximations from the analytic solution of the dam-break problem for the shallow water wave equations h_2 and u_2 . The results of this can be seen in Figure 15 for numerical solutions of \mathcal{V}_3 with $\Delta x = 10/2^9m$ to the smoothed dam-break problem at $t = 100s$ with $\alpha = 0.1m$ where h_0 is fixed and h_1 is varied.

We use a final time of $t = 100s$ as it allows the internal structure of the bore to develop more fully giving a more reliable mean estimate, as a consequence we resort to a coarser grid to keep the run-times reasonable. We find that decreasing Δx does not significantly alter the mean of u and h . We also find that increasing α also does not significantly alter the mean of h and u . Therefore, the mean behaviour of the converged conservative solution and thus the mean behaviour of the true solution of the Serre equations to the dam-break problem is captured by this numerical solution.

It can be seen that h_2 and u_2 are good approximations to the mean behaviour of the fluid inside the bore for a range of different aspect ratios. Although, as h_1/h_0 increases this approximation becomes worse, so that h_2 becomes an underestimate and u_2 becomes an overestimate.

We find that for $h_1/h_0 = 1.8$ the mean values of h and u inside the bore for the Serre equations are not equal to h_2 and u_2 . This can be seen in Figure 16 for the numerical solutions of \mathcal{V}_3 with $\Delta x = 10/2^9m$ to the smoothed dam-break problem with $\alpha = 0.1m$ at $t = 300s$. It can be seen that u_2 is an overestimate of u and h_2 is an underestimate of h , although the difference between these values and the mean behaviour of the Serre equations is small and only noticeable over long time periods.

The location of the leading wave of the Serre equations is poorly approximated by the location of the front of a bore in the shallow water wave equations. This is evident in \mathcal{V}_3 's numerical solution to the smoothed dam-break problem with $\alpha = 0.1m$ at $t = 300s$ using $\Delta x = 10/2^9m$, which is shown in Figure 17.

We note that the S_4 structure present in the numerical solutions using this method

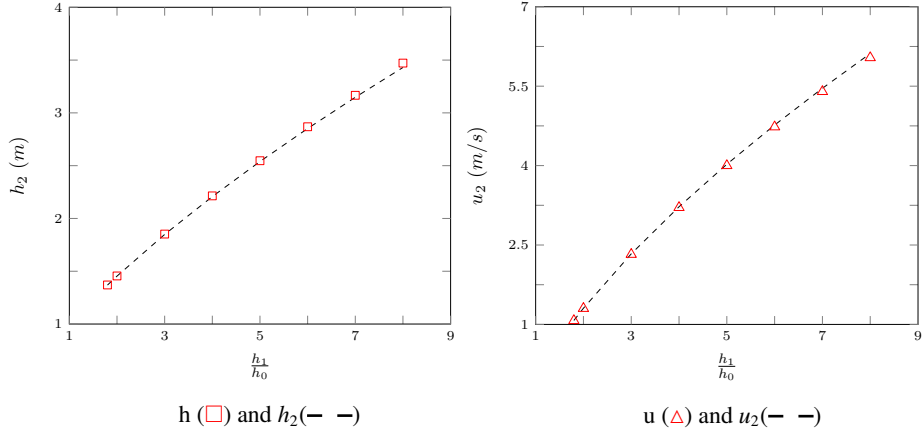


Figure 15: Comparison between mean behaviour inside the bore of the Serre equations and the analytic solution of the shallow water wave equations for a range of different aspect ratios.

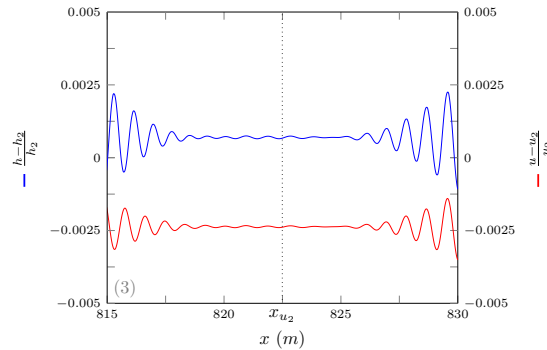


Figure 16: The relative difference between h and u and their comparisons h_2 and u_2 plotted around x_{u_2} for \mathcal{V}_3 's solutions with $\Delta x = 10/2^9 m$ for the smoothed dam-break problem with $\alpha = 0.1m$ at $t = 300s$.

and parameters at $t = 30s$ in Figure 11 has decayed away by $t = 300s$ in Figure 16. This is a trend throughout our numerical solutions where oscillation amplitude decreases over time around x_{u_2} , changing the structure of the solution. This can be seen by obtaining full convergence of the numerical solutions to the smoothed dam-break problem at $t = 3s$. The converged to numerical solutions for \mathcal{V}_3 are shown in Figure 18. From this figure it can be seen that the oscillation amplitudes for the numerical solutions for the smoothed dam-break problems with $\alpha = 0.4m$ and $\alpha = 0.1m$ are much larger at $t = 3s$ than they are at $t = 30s$ in Figure 4. Since we have demonstrated that our numerical solutions are good approximations to the true solution of the Serre equations at $t = 30s$ and $t = 3s$, decreasing oscillation amplitude around x_{u_2} over time must be a property of the Serre equations.

5.2.1. Contact discontinuity

El et al. [7] noted the presence of a ‘degenerate contact discontinuity’ which is the node in the \mathcal{S}_3 structure and travels at the mean fluid velocity in the bore.

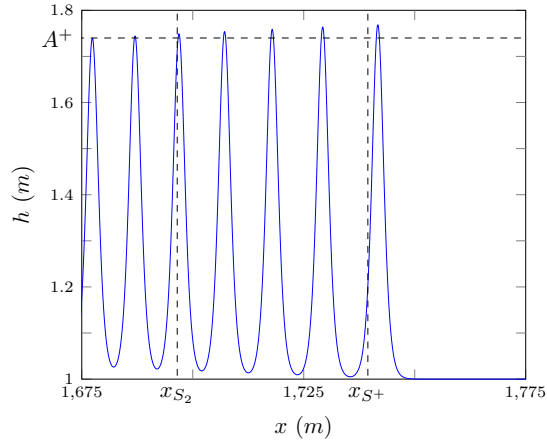


Figure 17: Numerical solution of \mathcal{V}_3 with $\Delta x = 10/2^9 m$ for the smoothed dam-break problem with $\alpha = 0.1m$ at $t = 300s$ around the front of the undular bore.

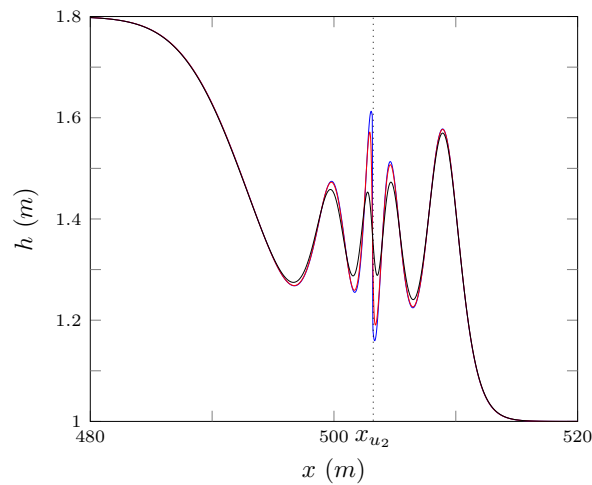


Figure 18: Numerical solution of \mathcal{V}_3 with $\Delta x = 10/2^{13} m$ for the smoothed dam-break problem with $\alpha = 0.001m$ (blue), $0.1m$ (red) and 0.4 (black) at $t = 3s$.

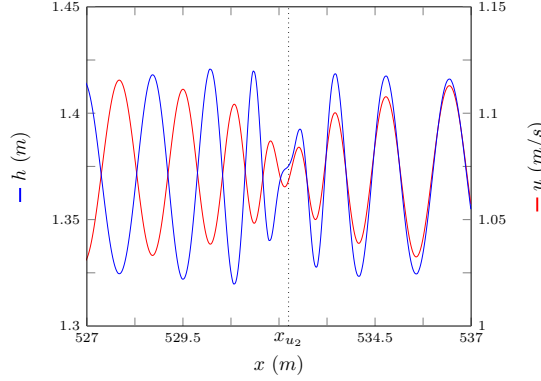


Figure 19: Numerical solution of \mathcal{V}_3 's with $\Delta x = 10/2^9 m$ for the smoothed dam-break problem with $\alpha = 0.1m$ at $t = 30s$ around the contact discontinuity.

We observe that as our numerical solutions evolve over time oscillations appear to be released from the contact discontinuity and travel away from it in both directions, leading to decay of amplitudes around the contact discontinuity. Therefore, the contact discontinuity is an important feature and its behaviour determines the structure of the oscillations in the middle of the undular bore.

The different speeds of the oscillations are determined by the phase velocity, which for the Serre equations linearised around the mean height \bar{h} and mean velocity \bar{u} in regions III and IV is

$$v_p = \bar{u} \pm \sqrt{g\bar{h}} \sqrt{\frac{3}{\bar{h}^2 k^2 + 3}} \quad (10)$$

with wave number k , it can be seen that as $k \rightarrow \infty$ then $v_p \rightarrow \bar{u}$ and as $k \rightarrow 0$ then $v_p \rightarrow \bar{u} \pm \sqrt{g\bar{h}}$. Since the contact discontinuity travels at the mean velocity inside the bore, it corresponds to very high wave number oscillations. The oscillations on the left travel slower than the contact discontinuity and are therefore lower wave number oscillations associated with the phase velocity $\bar{u} - \sqrt{g\bar{h}} \sqrt{3/(\bar{h}^2 k^2 + 3)}$. The oscillations on the right travel quicker than the contact discontinuity and are therefore lower wave number oscillations associated with the phase velocity $\bar{u} + \sqrt{g\bar{h}} \sqrt{3/(\bar{h}^2 k^2 + 3)}$.

These different phase velocities have two different behaviours for h and u . When the phase velocity is $\bar{u} + \sqrt{g\bar{h}} \sqrt{3/(\bar{h}^2 k^2 + 3)}$ we have oscillations where h and u are in-phase, while when the phase velocity is $\bar{u} - \sqrt{g\bar{h}} \sqrt{3/(\bar{h}^2 k^2 + 3)}$ we have oscillations where h and u are out-of-phase. This can be seen in Figure 19 for the numerical solutions of \mathcal{V}_3 with $\Delta x = 10/2^9 m$ for the smoothed dam-break problem with $\alpha = 0.1m$ at $t = 30s$.

5.3. Whitham Modulation Comparsion

El et al. [7] demonstrated that their Whitham modulation results approximated the numerical solutions of the smoothed dam-break problem well for a range of aspect

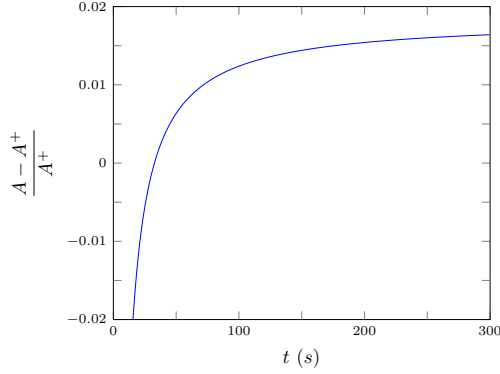


Figure 20: Relative difference between Whitham modulation result A^+ and the leading wave amplitude A from our numerical solutions of \mathcal{V}_3 with $\Delta x = 10/2^9 m$ for the smoothed dam-break problem with $\alpha = 0.1m$ over time.

490 ratios. However, we observe that the Whitham modulation results are an underestimate
491 compared to our numerical solutions.

492 This can be seen in Figure 20 as the relative difference between A^+ from El et al. [7]
493 and the leading wave amplitude of our numerical solution A does not converge to 0 over
494 time. Since we find that the numerical solutions for the smoothed dam-break problem
495 with $\alpha = 0.1m$ have converged for the front of the undular bore by $\Delta x = 10/2^8 m$ as
496 in Figure 11, our numerical solutions for A are considered reliable. We also note that
497 unlike the oscillations around x_{u_2} the leading wave amplitude increases over time.

498 The Whitham modulation results for the location of the leading wave x_{S^+} is a better
499 approximation than that given by the shallow water wave equations x_{S_2} , as can be seen
500 in Figure 17.

501 6. Conclusions

502 Utilising two finite difference methods of second-order and three finite difference
503 finite volume methods of various orders to solve the nonlinear weakly dispersive Serre
504 equations an investigation into the smoothed dam-break problem with varying steep-
505 ness was performed. Four different structures of the numerical solutions were observed
506 and demonstrated to be valid, the general trend of these structures is that an increase
507 in steepness increases the size and number of oscillations in the solution. This study
508 explains the different structures exhibited by the numerical results in the literature for
509 the smoothed dam-break problem for the Serre equations and uncovers a new result.
510 These results demonstrate that other methods in the literature could replicate our results
511 if their simulations are extended. Furthermore, these results suggest that this new result
512 and its associated structure is to be expected for the solution of the Serre equation to
513 the dam-break problem at least for short enough time spans.

514 We find that the analytical solution of the shallow water wave equations for the
515 dam-break problem provides a reasonable approximation to the mean height and veloc-
516 ity inside the bore formed by the smoothed dam-break problem for the Serre equations.
517 Finally, we observe that the Whitham modulations results for the leading wave of an

undular bore do not correspond with our validated numerical results, and are only an approximation. However, the Whitham modulation results do provide a more accurate approximation to the location of the front of an undular bore than the shallow water wave equations.

- [1] D. Mitsotakis, D. Dutykh, J. Carter, On the nonlinear dynamics of the traveling-wave solutions of the Serre system, *Wave Motion* 70 (1) (2017) 166–182.
- [2] O. Le Métayer, S. Gavrilyuk, S. Hank, A numerical scheme for the Green-Naghdi model, *Journal of Computational Physics* 229 (6) (2010) 2034–2045.
- [3] C. Zoppou, S. Roberts, J. Pitt, A Solution of the Conservation Law Form of the Serre Equations, *The ANZIAM Journal* 57 (4) (2017) 385–394.
- [4] C. Zoppou, J. Pitt, S. Roberts, Numerical Solution of the Fully Non-Linear Weakly Dispersive Serre Equations for Steep Gradient Flows, *Applied Mathematical Modelling* 48 (2017) 70–95.
- [5] P. Bonneton, E. Barthélémy, F. Chazel, R. Cienfuegos, D. Lannes, F. Marche, M. Tissier, Recent advances in Serre-Green Naghdi modelling for wave transformation, breaking and runup processes, *European Journal of Mechanics B/Fluids* 30 (6) (2011) 589–597.
- [6] P. Bonneton, F. Chazel, D. Lannes, F. Marche, M. Tissier, A splitting approach for the fully nonlinear and weakly dispersive Green-Naghdi model, *Journal of Computational Physics* 230 (4) (2011) 1479–1498.
- [7] G. El, R. H. J. Grimshaw, N. F. Smyth, Unsteady undular bores in fully nonlinear shallow-water theory, *Physics of Fluids* 18 (2) (2006) 027104.
- [8] D. Mitsotakis, B. Ilan, D. Dutykh, On the Galerkin/Finite-Element Method for the Serre Equations, *Journal of Scientific Computing* 61 (1) (2014) 166–195.
- [9] C. H. Su, C. S. Gardner, Korteweg-de Vries equation and generalisations. III. Derivation of the Korteweg-de Vries equation and Burgers equation, *Journal of Mathematical Physics* 10 (3) (1969) 536–539.
- [10] D. Lannes, P. Bonneton, Derivation of asymptotic two-dimensional time-dependent equations for surface water wave propagation, *Physics of Fluids* 21 (1) (2009) 16601–16610.
- [11] M. Li, P. Guyenne, F. Li, L. Xu, High order well-balanced CDG-FE methods for shallow water waves by a Green-Naghdi model, *Journal of Computational Physics* 257 (2014) 169–192.
- [12] Y. A. Li, Hamiltonian Structure and Linear Stability of Solitary Waves of the Green-Naghdi Equations, *Journal of Nonlinear Mathematical Physics* 9 (2002) 99–105.
- [13] A. E. Green, P. M. Naghdi, A derivation of equations for wave propagation in water of variable depth, *Journal of Fluid Mechanics* 78 (2) (1976) 237–246.

- 556 [14] C. Wu, G. Huang, Y. Zheng, Theoretical solution of dam-break shock wave, Journal
557 of Hydraulic Engineering 125 (11) (1999) 1210–1215.
- 558 [15] A. A. Harten, High resolution schemes for hyperbolic conservation laws, Journal
559 of Computational Physics 49 (3) (1983) 357–393.
- 560 [16] G. El, M. Hoefer, Dispersive shock waves and modulation theory, Physica D:
561 Nonlinear Phenomena 333 (2016) 11–65.

562 **Appendix A.**

563 The methods \mathcal{E} and \mathcal{D} use the centred second-order finite difference approximation
 564 to the momentum equation (1b), denoted as \mathcal{D}_u . For the mass equation (1a) \mathcal{E} uses the
 565 two step Lax-Wendroff method, denoted as \mathcal{E}_h while \mathcal{D} uses a centred second-order
 566 finite difference approximation, denoted as \mathcal{D}_h .

567 *Appendix A.1. \mathcal{D}_u for the Momentum Equation*

568 First (1b) is expanded to get

$$569 \quad h \frac{\partial u}{\partial t} - h^2 \frac{\partial^2 u}{\partial x \partial t} - \frac{h^3}{3} \frac{\partial^3 u}{\partial x^2 \partial t} = -X \quad (\text{A.1})$$

571 where X contains only spatial derivatives and is

$$572 \quad X = uh \frac{\partial u}{\partial x} + gh \frac{\partial h}{\partial x} + h^2 \frac{\partial u}{\partial x} \frac{\partial u}{\partial x} + \frac{h^3}{3} \frac{\partial u}{\partial x} \frac{\partial^2 u}{\partial x^2} - h^2 u \frac{\partial^2 u}{\partial x^2} - \frac{h^3}{3} u \frac{\partial^3 u}{\partial x^3}. \quad (\text{A.2})$$

574 All derivatives are approximated by second-order centred finite difference approximations
 575 on a uniform grid in space and time, which after rearranging into an update
 576 formula becomes

$$577 \quad h_i^n u_i^{n+1} - (h_i^n)^2 \left(\frac{u_{i+1}^{n+1} - u_{i-1}^{n+1}}{2\Delta x} \right) - \frac{(h_i^n)^3}{3} \left(\frac{u_{i+1}^{n+1} - 2u_i^{n+1} + u_{i-1}^{n+1}}{\Delta x^2} \right) = -Y_i^n \quad (\text{A.3})$$

579 where

$$580 \quad Y_i^n = 2\Delta t X_i^n - h_i^n u_i^{n-1} + (h_i^n)^2 \left(\frac{u_{i+1}^{n-1} - u_{i-1}^{n-1}}{2\Delta x} \right) + \frac{(h_i^n)^3}{3} \left(\frac{u_{i+1}^{n-1} - 2u_i^{n-1} + u_{i-1}^{n-1}}{\Delta x^2} \right)$$

582 and

$$583 \quad X_i^n = u_i^n h_i^n \frac{u_{i+1}^n - u_{i-1}^n}{2\Delta x} + gh_i^n \frac{h_{i+1}^n - h_{i-1}^n}{2\Delta x} + (h_i^n)^2 \left(\frac{u_{i+1}^n - u_{i-1}^n}{2\Delta x} \right)^2$$

$$584 \quad + \frac{(h_i^n)^3}{3} \frac{u_{i+1}^n - u_{i-1}^n}{2\Delta x} \frac{u_{i+1}^n - 2u_i^n + u_{i-1}^n}{\Delta x^2} - (h_i^n)^2 u_i^n \frac{u_{i+1}^n - 2u_i^n + u_{i-1}^n}{\Delta x^2}$$

$$585 \quad - \frac{(h_i^n)^3}{3} u_i^n \frac{u_{i+2}^n - 2u_{i+1}^n + 2u_{i-1}^n - u_{i-2}^n}{2\Delta x^3}.$$

588 Equation (A.3) can be rearranged into an explicit update scheme \mathcal{D}_u for u given its
 589 current and previous values, so that

$$590 \quad \begin{bmatrix} u_0^{n+1} \\ \vdots \\ u_m^{n+1} \end{bmatrix} = A^{-1} \begin{bmatrix} -Y_0^n \\ \vdots \\ -Y_m^n \end{bmatrix} =: \mathcal{D}_u(\mathbf{u}^n, \mathbf{h}^n, \mathbf{u}^{n-1}, \Delta x, \Delta t) \quad (\text{A.4})$$

592 where A is a tri-diagonal matrix.

593 *Appendix A.2. Numerical Methods for the Mass Equation*

594 The two step Lax-Wendroff update \mathcal{E}_h for h is

$$595 \quad h_{i+1/2}^{n+1/2} = \frac{1}{2} (h_{i+1}^n + h_i^n) - \frac{\Delta t}{2\Delta x} (u_{i+1}^n h_{i+1}^n - h_i^n u_i^n), \\ 596 \\ 597$$

$$598 \quad h_{i-1/2}^{n+1/2} = \frac{1}{2} (h_i^n + h_{i-1}^n) - \frac{\Delta t}{2\Delta x} (u_i^n h_i^n - h_{i-1}^n u_{i-1}^n) \\ 599$$

600 and

$$601 \quad h_i^{n+1} = h_i^n - \frac{\Delta t}{\Delta x} (u_{i+1/2}^{n+1/2} h_{i+1/2}^{n+1/2} - u_{i-1/2}^{n+1/2} h_{i-1/2}^{n+1/2}). \\ 602$$

603 The quantities $u_{i\pm 1/2}^{n+1/2}$ are calculated using u^{n+1} obtained by applying \mathcal{D}_u (A.4) to u^n
604 then linearly interpolating in space and time to give

$$605 \quad u_{i+1/2}^{n+1/2} = \frac{u_{i+1}^{n+1} + u_{i+1}^n + u_i^{n+1} + u_i^n}{4} \\ 606$$

607 and

$$608 \quad u_{i-1/2}^{n+1/2} = \frac{u_i^{n+1} + u_i^n + u_{i-1}^{n+1} + u_{i-1}^n}{4}. \\ 609$$

610 Thus we have the following update scheme \mathcal{E}_h for (1a)

$$611 \quad \mathbf{h}^{n+1} = \mathcal{E}_h(\mathbf{u}^n, \mathbf{h}^n, \mathbf{u}^{n+1}, \Delta x, \Delta t). \quad (\text{A.5}) \\ 612$$

613 The second order centered finite difference approximation to the conservation of
614 mass equation (1a) is

$$615 \quad h_i^{n+1} = h_i^{n-1} - \Delta t \left(u_i^n \frac{h_{i+1}^n - h_{i-1}^n}{\Delta x} + h_i^n \frac{u_{i+1}^n - u_{i-1}^n}{\Delta x} \right). \\ 616$$

617 Thus we have an update scheme \mathcal{D}_h for all i

$$618 \quad \mathbf{h}^{n+1} = \mathcal{D}_h(\mathbf{u}^n, \mathbf{h}^n, \mathbf{h}^{n-1}, \Delta x, \Delta t). \quad (\text{A.6}) \\ 619$$

620 *Appendix A.3. Complete Method*

621 The method \mathcal{E} is the combination of (A.5) for (1a) and (A.4) for (1b) in the follow-
622 ing way

$$623 \quad \begin{aligned} \mathbf{u}^{n+1} &= \mathcal{D}_u(\mathbf{u}^n, \mathbf{h}^n, \mathbf{u}^{n-1}, \Delta x, \Delta t) \\ 624 \quad \mathbf{h}^{n+1} &= \mathcal{E}_h(\mathbf{u}^n, \mathbf{h}^n, \mathbf{u}^{n+1}, \Delta x, \Delta t) \end{aligned} \left\{ \mathcal{E}(\mathbf{u}^n, \mathbf{h}^n, \mathbf{u}^{n-1}, \mathbf{h}^{n-1}, \Delta x, \Delta t) \right. \quad (\text{A.7})$$

625 The method \mathcal{D} is the combination of (A.6) for (1a) and (A.4) for (1b) in the follow-
626 ing way

$$627 \quad \begin{aligned} \mathbf{h}^{n+1} &= \mathcal{D}_h(\mathbf{u}^n, \mathbf{h}^n, \mathbf{h}^{n-1}, \Delta x, \Delta t) \\ 628 \quad \mathbf{u}^{n+1} &= \mathcal{D}_u(\mathbf{u}^n, \mathbf{h}^n, \mathbf{u}^{n-1}, \Delta x, \Delta t) \end{aligned} \left\{ \mathcal{D}(\mathbf{u}^n, \mathbf{h}^n, \mathbf{u}^{n-1}, \mathbf{h}^{n-1}, \Delta x, \Delta t) \right. \quad (\text{A.8})$$